



Weight Function Procedure for Reduced Order Fracture Analysis of Arbitrary Flaws in Cylindrical Pressure Vessels

August 2022

Changing the World's Energy Future

Benjamin W Spencer, William M Hoffman, Wen Jiang



DISCLAIMER

This information was prepared as an account of work sponsored by an agency of the U.S. Government. Neither the U.S. Government nor any agency thereof, nor any of their employees, makes any warranty, expressed or implied, or assumes any legal liability or responsibility for the accuracy, completeness, or usefulness, of any information, apparatus, product, or process disclosed, or represents that its use would not infringe privately owned rights. References herein to any specific commercial product, process, or service by trade name, trade mark, manufacturer, or otherwise, does not necessarily constitute or imply its endorsement, recommendation, or favoring by the U.S. Government or any agency thereof. The views and opinions of authors expressed herein do not necessarily state or reflect those of the U.S. Government or any agency thereof.

Weight Function Procedure for Reduced Order Fracture Analysis of Arbitrary Flaws in Cylindrical Pressure Vessels

Benjamin W Spencer, William M Hoffman, Wen Jiang

August 2022

**Idaho National Laboratory
Idaho Falls, Idaho 83415**

<http://www.inl.gov>

**Prepared for the
U.S. Department of Energy
Under DOE Idaho Operations Office
Contract DE-AC07-05ID14517**

Weight Function Procedure for Reduced Order Fracture Analysis of Arbitrary Flaws in Cylindrical Pressure Vessels

Benjamin W. Spencer^{a,*}, William M. Hoffman^b, Wen Jiang^a

^aComputational Mechanics and Materials, Idaho National Laboratory, P.O. Box 1625, Idaho Falls, ID 83415-3840

^bSpecial Reactor Concepts, Idaho National Laboratory, P.O. Box 1625, Idaho Falls, ID 83415-3840

Abstract

Fracture mechanics calculations using the finite element method can be computationally expensive, which makes them challenging to use in engineering evaluations of flaws in pressure vessels. The weight function (WF) technique is a reduced order fracture modeling method that is widely used to greatly reduce these computational costs. Its computational efficiency is essential for use in probabilistic fracture mechanics evaluations of embrittled nuclear reactor pressure vessels (RPVs), due to the large number of sampled flaws that must be evaluated. Although the WF technique is general, it is typically used only for axis-aligned flaws. Recent discoveries of off-axis flaws in operating nuclear reactors have necessitated detailed simulations of such flaws and the interactions between neighboring flaws. This paper presents a generalized WF approach applicable for analyzing arbitrary flaw geometries in thick-walled cylindrical vessels, including surface-breaking and subsurface flaws, which can either axis-aligned or off-axis, and can account for interactions with other flaws. This approach is demonstrated on representative simulations of multiple flaw geometries in a RPV subjected to transient loading conditions. In all cases, the WF technique gives good comparison with benchmark results from direct simulation with greatly reduced computational effort.

Keywords: Weight Function, Fracture Mechanics, Extended Finite Element Method, Off-Axis Flaw, Mixed-Mode Fracture, Interacting Flaws

1. Introduction

Linear elastic fracture mechanics (LEFM) is widely used to assess fracture at flaws in both deterministic and probabilistic assessments of pressure vessel integrity. The procedures for evaluating stress intensity factors (SIFs) for arbitrary flaw geometries are well established. The finite element method (FEM) is arguably the most widely used numerical technique for solving this class of problem, and it permits the creation of arbitrary meshes to represent the geometry of the pressure vessel and flaw under consideration. Using standard FEM, meshes can be created that conform to the geometry of the flaw, while the more recently developed extended finite element method (XFEM) [1] permits the definition of arbitrary mesh-independent fractures, thus alleviating some of the complexity in mesh generation. Domain integral procedures are well established for evaluating energy release rates and mixed-mode SIFs [2].

Setting up and running finite element simulations of flaws can be complex and computationally expensive, especially for three-dimensional (3D) models. In practice, many flaw geometries of interest can be characterized using standardized geometric approximations such as elliptical shapes. The weight

function (WF) technique [3, 4] significantly reduces the effort required for analyzing standardized flaw geometries, as it permits the solution for a given flaw geometry to be performed once and then reused for a variety of loading conditions. Once the stress field is computed using a global model of the pressure vessel of interest, SIFs can be computed via the WF approach. This involves first fitting a polynomial to describe the through-wall distribution of the relevant far-field stress component. The products of the polynomial coefficients with their corresponding stress intensity factor influence coefficients (SIFICs) are then summed to obtain the SIFs, a process that requires minimal computational resources.

The WF approach has been used for a variety of loading conditions and flaw geometries for mode-*I* [5, 6, 7] loading, and in a more limited way for mixed-mode loading [8, 9]. A WF-based approach is adopted in the current (2021) version of Section XI, Nonmandatory Appendix A, Article A-3000, “Method of K_I Determination” in the ASME Boiler & Pressure Vessel Code [10] (hereafter referred to as ASME Section XI) for both axis-aligned elliptical and semi-elliptical flaws in nuclear light-water reactor (LWR) pressure vessels. The American Petroleum Institute API 579-1 standard [11] also employs a WF-based approach for crack-like flaws.

The methods for determining K_I in ASME Section XI have evolved over time. SIFICs have long been employed for surface-breaking flaws, with closed-form expressions provided for computing SIFICs up to 4th order based on tables of coefficients provided for various flaw geometries, with provisions to interpo-

*Corresponding author

Email address: benjamin.spencer@inl.gov (Benjamin W. Spencer)

¹This article is published as: B. W. Spencer, W. M. Hoffman, and W. Jiang. Weight function procedure for reduced order fracture analysis of arbitrary flaws in cylindrical pressure vessels. *International Journal of Pressure Vessels and Piping*, 200:104784, Aug. 2022. DOI:10.1016/j.ijpvp.2022.104784

late those coefficients for other flaw geometries. As described in [12], in the 2015 code, separate methods were provided for computing SIFs for inside-surface circumferential flaws and flaws in flat plates. In 2017, the code was expanded to include methods for inside- and outside-surface axial flaws.

For subsurface flaws, a WF-based approach was first introduced in the 2015 code. Prior to that, a procedure for computing K_I based on superposition of contributions from membrane and bending stresses was employed, using geometry-dependent correction factors that were obtained from graphical plots. A closed-form approach for computing K_I consistent with this procedure that avoids the need for plot lookups was developed in [13]. The WF approach introduced starting in 2015 provides tabular values for coefficients used in SIF calculation, based on a set of solutions developed by [14]. These tabulated values were initially for a limited set of flaw geometries that notably did not include near-surface flaws, but based on the work of [15], the 2021 code includes an expanded set of solutions for most flaws except for those very near the vessel surfaces. In the work of [14], the authors benchmarked their solutions against multiple solutions for subsurface flaws in plates, including classical analytical solutions for membrane loading [16, 17, 18] and the WF-based API 579 solutions.

The WF approach is particularly helpful in integrity assessments of LWR pressure vessels. These reactor pressure vessels (RPVs) contain the reactor core and form an essential boundary against fission product release during both normal and off-normal conditions. RPVs contain potentially large populations of flaws introduced during the manufacturing process. As reactors age, the steel comprising the RPV becomes more brittle due to long-term exposure to irradiation and elevated temperatures. Because of the large number of flaws and the uncertainties inherent in characterizing the flaw population, probabilistic fracture mechanics (PFM) techniques based on Monte Carlo sampling are used to assess the integrity of embrittled RPVs. Probabilistic sampling can involve very large numbers of flaw evaluations, so the ability to rapidly evaluate SIFs is essential for efficient computations.

PFM evaluations of embrittled RPVs routinely utilize WF techniques to evaluate SIFs. For example, the Fracture Analysis of Vessels – Oak Ridge (FAVOR) code [19, 20] is one of the most widely used codes for this application. FAVOR uses the WF approach to evaluate SIFs in semi-elliptical surface-breaking flaws, including the effects of cladding. For embedded (i.e., subsurface) flaws, FAVOR uses the pre-2015 ASME Section XI approach based on bending and membrane stresses, using the closed-form methods of [13]. This type of PFM analysis has typically been limited to axis-aligned flaws.

Recent events have led to increased interest in the analysis of off-axis flaws in RPVs. In 2012, inspections of the RPVs at the Belgian Doel 3 and Tihange 2 reactors indicated the presence of thousands of flaws with laminar (parallel to the RPV surfaces) or quasi-laminar (tilted slightly off-parallel to the surface) orientations [21, 22]. These two reactors were shut down for an extensive period of time before ultimately being restarted after detailed assessments of the safety consequences of these findings had been conducted [23]. Direct 3D fracture simulations were

required to study off-axis flaws and the interactions between flaws. XFEM is readily applicable to such problems [23, 24, 25] and alleviates some of the difficulty in defining flaw geometries. However, 3D XFEM models of flaws still require significant computational resources, even for deterministic modeling, making PFM assessments of flaw populations that include off-axis flaws unfeasible with current computing resources.

Motivated by the need for efficient methods of evaluating arbitrary flaw geometries in RPVs, this paper presents a generalization of the WF methodology to evaluate fracture parameters for flaws with arbitrary geometries in cylindrical thin- or thick-walled pressure vessels. The WF methodology used in practice for axis-aligned flaws only considers the distribution of the component of stress normal to the flaw (hoop stresses for axial flaws or axial stresses for circumferential flaws) because the stresses in other directions do not affect the mode-*I* SIF (K_I). The SIFs for off-axis flaws, however, are affected by the hoop, radial, and axial stresses. The basic concept of the WF methodology is generally applicable to any combination of loading systems, including loading in multiple directions. Here, this property of WFs is exploited to extend the standard procedure to include the effects of multiaxial loading, which allows it to be used to obtain SIFs for general flaw geometries in cylindrical vessels.

This work uses the Grizzly [26, 27] code, a general-purpose simulation tool developed under the U.S. Department of Energy’s Light Water Reactor Sustainability program to address a variety of aging mechanisms in nuclear power plant structures. Grizzly provides a modular, flexible framework for PFM that allows it to take advantage of parallel computing resources to efficiently evaluate large populations of flaws, and permits it to address effects (e.g., cold plumes near inlets) that are difficult to address with other PFM codes. The goal of the generalized WF approach presented here is to permit the inclusion of off-axis and interacting flaws in the same type of PFM analysis currently performable on populations of axis-aligned flaws.

In Section 2, this paper presents a review of the WF methodology used in current practice for axis-aligned flaws. This review provides the basis for the generalized WF approach that is described in Section 3. In this work, XFEM is used to represent the presence of the discontinuities introduced by the flaws, and Section 4 summarizes the XFEM approach used in this work. Examples of applying this technique are presented in Section 5, first for axis-aligned flaws and then for general flaw geometries, including an off-axis flaw and multiple interacting flaws.

2. Weight Function Procedure for Axis-Aligned Flaws

The core principle of the WF approach, which was originally proposed by Buckner [3] and expanded on by Rice [4], is that the SIF (K_I in the case of mode-*I* loading) can be expressed as a linear combination of the products of a set of stress coefficients, w_i , and corresponding SIFs, K_i :

$$K_I = \sum_{i=0}^n w_i K_i \quad (1)$$

where w_i is a multiplier applied to a given ‘‘load system’’ that defines a far-field stress distribution that would occur in the uncracked structure under a specific set of boundary conditions (BCs). K_I is the SIF resulting from the application of load system i . The number of load systems is $n - 1$.

This technique assumes that the presence of the flaw does not affect the far-field stresses, and that the contributions of individual terms in a polynomial expansion of the far-field stress to the SIF can be superimposed to compute that SIF under an arbitrary stress field. The superposition principle underlying this method is applicable to any linear system, and is thus applicable to LEFM.

There is considerable flexibility in the selection of load systems to describe the far-field stress. The load systems are not strictly required to be orthogonal to each other, though the process of determining the coefficients, w_i , to describe an arbitrary stress field is simplified if they are. As long as the far-field stress applied to a crack can be accurately described as a linear combination of multiple load states, Equation 1 accurately describes K_I . In practice, for mode- I loading of axis-aligned flaws in pressure vessels, the spatial variation of the far-field stress normal to the flaw is approximated using a fitted polynomial. If this stress is denoted as $\bar{\sigma}$ and the radial distance from the inner surface is r , this polynomial expansion is expressed as:

$$\bar{\sigma}(r) = \sum_{i=0}^n w_i (r/t)^i \quad (2)$$

where t is the total wall thickness. The polynomial order is indicated by n . Cubic ($n = 3$) or fourth-order ($n = 4$) polynomials are typically sufficient for engineering accuracy. The set of w coefficients that describe the polynomial form of the through-wall stress variation can be used together with appropriate SIFICs (discussed below) in Equation 1 to compute K_I .

The values of the SIFICs (K_I) are functions of the geometry of the crack and the component containing it, as well as the applied load state. To compute a given SIFIC, K_I , one evaluates K_I using an analytic or numerical model of the geometry of interest under load state i . As justified by the principle of superposition [5] and illustrated in Figure 1, a SIFIC due to a load state obtained by applied far-field surface tractions is equivalent to that obtained by applying the tractions that would be present at the crack surface from that same load state were the crack not present in the body. Applying crack-face tractions may be more convenient than applying the BCs needed to obtain a desired load state, but because these two approaches are equivalent, they can be used interchangeably. If the polynomial form of Equation 2 is used to represent the load systems, the applied loadings would vary spatially through the wall according to the order of the terms in the polynomial corresponding to a given load system.

A numerical model with sufficient refinement to accurately compute K_I typically requires many degrees of freedom. Because the WF approach represents the figure of merit from a complex numerical model in terms of a small set of parameters, it can be considered a type of reduced order model.

By developing a set of computational models for a variety

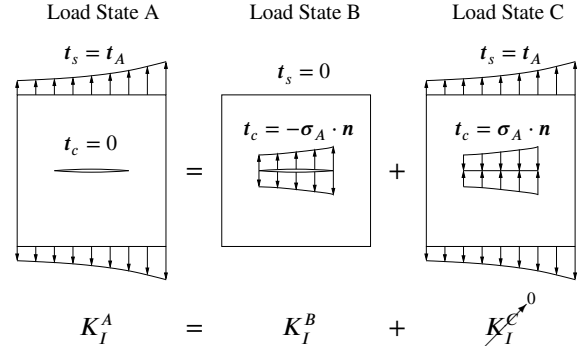


Figure 1: Application of the principle of superposition [5] to demonstrate the equivalence of K_I resulting from tractions applied to a boundary of the model, t_s (Load State A), to the K_I that would result from applying crack-face tractions, t_c , that would exist in Load State A at the location of the crack if that crack was not present (Load State B). The applied surface tractions of Load State A are denoted as t_A , and the tractions at the crack location in Load State A if that crack was not present are expressed as $\sigma_A \cdot n$, where σ_A is the stress field from Load State A in the absence of a crack, and n is the unit vector normal to the crack surface pointing outward from the body. Because the crack is exactly closed by Load State C, its corresponding SIF (K_I^C) is zero, thus $K_I^A = K_I^B$. (Figure based on [20]).

of flaw and component geometries, one can develop a database of SIFICs. Interpolation or fitted equations can be used to describe the dependencies of these SIFICs on the relevant parameters within the domain of applicability. Such a database can cover a wide variety of conditions, and using SIFICs from a database rather than direct solutions greatly reduces the computational burden for fracture analysis. ASME Section XI provides closed-form expressions and tabular data for SIFICs for a variety of circumferential and axial elliptical and semi-elliptical flaws in thin- or thick-walled cylinders and plates. These are used to various extents by the FAVOR and Grizzly codes for PFM considering axis-aligned flaws.

It is important to note that the WF approach can even significantly reduce the computational effort for a single evaluation of a specific flaw geometry. A single computational step is required to generate each SIFIC, and a small number of load states are typically required to represent the loading conditions on a crack. For example, four load states are required to be analyzed if the stress is represented by a cubic polynomial. Analyses of transient loading conditions in pressure vessels often requires hundreds of simulation time steps. A direct approach to evaluating the K_I history during a transient could involve hundreds of time steps, while an equivalent WF result could be obtained using only four evaluations of the detailed fracture model to determine the SIFICs. These SIFICs would be used in conjunction with a much less computationally expensive model of the structure without the fracture present to compute the evolution of the through-wall stress distribution.

3. Multi-Axial Weight Function Procedure for Off-Axis Flaws

To expand the WF procedure used for axis-aligned flaws in cylindrical vessels, provisions must be made for an expanded set

of WFs that represent the spatial distribution of multiple components of the stress, rather than just the component of the stress normal to the flaw, as is the case for axis-aligned flaws. The applied far-field stress, still denoted as $\bar{\sigma}$ for this general case, is no longer necessarily normal to the flaw. In a pressure vessel subjected to loading conditions that are relatively uniform spatially, the principal stresses are aligned with the major axes of the vessel, so the stress field can be represented by the through-wall variation of the axial, hoop, and radial components of the stress. If cubic polynomials are used to independently represent the variation of these three components of stress, the full stress field can be represented using 12 weight functions: four for each of the three stress components. Fourth-order polynomials require five weight functions for each direction, for a total of 15 weight functions.

Figure 2 illustrates the 12 stress coefficients required for using cubic polynomials and the way in which K_I can be computed as a summation of the products of those stress coefficients and their corresponding SIFs, demonstrating how Equation 1 can be applied for this multiaxial loading system. For axis-aligned flaws, K_I is only affected by one component of the stress, thereby simplifying to the standard approach; however, off-axis flaw calculations potentially involve all three stress components.

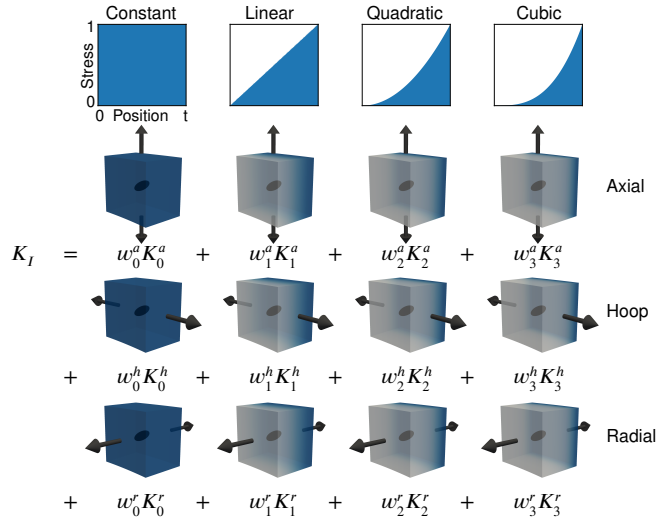


Figure 2: Multi-axial application of the WF method of Equation 1 for cylinders. Orthogonal load systems corresponding to terms in a cubic polynomial are used to independently describe the spatial variation of the axial, hoop, and radial stress (denoted by corresponding a , h , and r superscripts on the stress coefficients, w , and SIFs, K). The top row illustrates the stress magnitudes as a function of through-thickness position. A through-wall segment of the cylindrical vessel is shown for each load system (with the inner surface facing to the left), shaded according to the magnitude of the stress component.

The process of computing the SIFs for this multiaxial system follows the same philosophy as for a uniaxial system. A given SIF is the SIF resulting from application of the corresponding loading system. In the present work, this is computed numerically by evaluating the interaction integral for the SIFs of interest under each loading system. The load systems consist

of various configurations of far-field stress states, which can be applied to the numerical model by either developing a set of BCs that result in the desired stress state (as in Load State A in Figure 1), or by applying corresponding crack-face tractions (as in Load State B in Figure 1). Either approach would give the same result, but in this work, the choice was made to apply the far-field stresses rather than surface tractions on the crack faces, for implementational convenience. This avoids the need to apply surface tractions in arbitrary directions to the crack faces. Also, terms involving those applied surface tractions must be included in the fracture integrals. Both of these tasks are certainly possible with XFEM, which is used to represent fractures in the present work, but present some implementational challenges that are avoided if far-field stresses are applied instead.

Applying far-field stresses also presents certain challenges in that for the load systems in the three directions to be orthogonal, each load system must result in nonzero stresses in the desired direction, and zero stresses in all other directions. Intuitively, one might expect to be able to achieve stress fields that vary spatially in accordance with the desired polynomial forms by applying spatially varying surface tractions to the appropriate boundaries of the model domain. However, due to Saint-Venant's principle, at a sufficient distance from those boundaries, the higher-order variation in the fields is lost, and the stress field in the body at the location of the crack does not match the polynomial form of the applied boundary condition.

The desired stress fields can, however, be obtained by fixing the far-field surfaces in the directions normal to the desired stress component and applying appropriately defined eigenstrains (i.e., intrinsically induced strains such as those that occur during thermal expansion [28]) throughout the domain. The component of the eigenstrain tensor in the direction of the prescribed far-field stress, $\bar{\sigma}$, for a given load system is simply $\bar{\sigma}/E$, where E is the elastic modulus. To counteract the strains induced by Poisson's effect, the components in the orthogonal directions should be $-\nu\bar{\sigma}/E$. For example, in a cylinder in which the radial, azimuthal, and axial directions are denoted as r , θ , and z respectively, the following nonzero components of an applied eigenstrain tensor that results in the desired $\bar{\sigma}$ for the axial direction would be applied:

$$\begin{aligned} \epsilon_{zz} &= \frac{\bar{\sigma}}{E} \\ \epsilon_{rr} = \epsilon_{\theta\theta} &= \frac{-\nu\bar{\sigma}}{E} \end{aligned} \quad (3)$$

The same procedure is also applicable for computing the eigenstrain for the azimuthal and radial directions. However, for the load systems in those two directions, an additional body force must also be applied to maintain equilibrium. This body force can be derived from the full set of equations of equilibrium for thick-walled cylinders in cylindrical coordinates, which are

expressed as [29]:

$$\begin{aligned} \frac{\partial \sigma_{rr}}{\partial r} + \frac{1}{r} \frac{\partial \sigma_{r\theta}}{\partial \theta} + \frac{\partial \sigma_{rz}}{\partial z} + \frac{\sigma_{rr} - \sigma_{\theta\theta}}{r} + b_r &= 0 \\ \frac{\partial \sigma_{r\theta}}{\partial r} + \frac{1}{r} \frac{\partial \sigma_{\theta\theta}}{\partial \theta} + \frac{\partial \sigma_{\theta z}}{\partial z} + 2 \frac{\sigma_{r\theta}}{r} + b_\theta &= 0 \\ \frac{\partial \sigma_{rz}}{\partial r} + \frac{1}{r} \frac{\partial \sigma_{\theta z}}{\partial \theta} + \frac{\partial \sigma_{zz}}{\partial z} + \frac{\sigma_{rz}}{r} + b_z &= 0 \end{aligned} \quad (4)$$

where the b terms are body forces. If it is assumed that the stress state only varies in the radial direction, and not in the z or θ direction, the shear stresses are zero. In the above equilibrium equations for the hoop and axial directions, this assumption leads to $b_\theta = 0$ and $b_z = 0$, respectively, while the following non-trivial equation remains for equilibrium in the radial direction:

$$b_r = -\frac{\partial \sigma_{rr}}{\partial r} - \frac{\sigma_{rr} - \sigma_{\theta\theta}}{r} \quad (5)$$

For the vessel wall to be in a state of equilibrium, this shows that, if a radial or hoop stress is induced via an applied eigenstrain, a nonzero radial body force per unit volume b_r must be applied.

For the load systems in which only a radial stress is applied ($\sigma_{rr} = \bar{\sigma}$), this leads to:

$$b_r = -\frac{\partial \bar{\sigma}}{\partial r} - \frac{\bar{\sigma}}{r} \quad (6)$$

The corresponding expression for load systems in which only a hoop stress is applied ($\sigma_{\theta\theta} = \bar{\sigma}$) leads to:

$$b_r = \frac{\bar{\sigma}}{r} \quad (7)$$

Because Equation 5 does not involve the axial stress (σ_{zz}), no application of body forces is required for axial loading.

Finally, appropriate BCs are prescribed to enforce no displacement normal to the loading. There is no need for special treatment for the hoop loading because the no-displacement BCs imposed for a wedge model already enforce that condition. For the axial loading state, no-displacement BCs are imposed in the vertical direction on the top and bottom surfaces of the model, and for the radial loading state, no-displacement BCs are imposed normal to the inner and outer surfaces of the vessel.

To summarize, the procedure for developing the SIFs used for the WF approach for an arbitrary off-axis flaw first involves creating a model of the flaw of interest in a sufficiently large section of the cylindrical vessel wall, with sufficient refinement to accurately compute fracture solutions. This model must represent the vessel and flaw geometry of interest. To calculate the through-wall stress variation with cubic polynomials, the flaw model is subjected to 12 different loading configurations for the three stress components and the four terms in the polynomial for each of those stress components. For quartic polynomials, 15 loading configurations are required. For each loading state, a spatially varying eigenstrain of the form shown in Equation 3 is applied. Appropriate BCs are also prescribed for each load system as described above. For the loading states in the radial and hoop directions, the appropriate body force following Equation 6 or 7 is applied to maintain equilibrium.

It should be noted that if the model used for SIFIC generation is properly set up and no crack is present in the model, the model should be in equilibrium under the prescribed eigenstrains and body forces, meaning that the displacements due to each of these load states should be exactly zero. Once a crack is introduced into the model, local variations to the stress field will occur in the vicinity of that crack.

When the flaw models are subjected to these load states, the SIFs are obtained by evaluating the SIFs of interest. These could include K_I , K_{II} , and K_{III} , as well as other LFM parameters of interest (e.g., the T -stress). This procedure could be used to generate SIFs for any other fracture parameter of interest, as long as it is a linear function of the loading and the principle of superposition applies to its computation. Once these SIFs are obtained, an appropriate global model of the RPV with no flaw is used to obtain the far-field stresses. A polynomial fitting is performed on the far-field stresses to obtain the stress coefficients, and K_I is computed for each load step from the stress coefficients and SIFs using Equation 1.

4. Extended Finite Element Method and Interaction Integrals for Fracture Computations

The XFEM approach, as originally proposed in [30, 31], enriches the standard continuous finite element interpolation of the solution field, \mathbf{u} , as a function of spatial coordinate, \mathbf{x} , and time, t , with Heaviside and near-tip enrichment functions:

$$\mathbf{u}(\mathbf{x}, t) = \underbrace{\sum_{I=1}^n N_I(\mathbf{x}) \mathbf{u}_I(t)}_{\text{Continuous}} + \underbrace{\sum_{J=1}^n N_J(\mathbf{x}) H(\mathbf{x}) \mathbf{b}_J(t)}_{\text{Heaviside Enriched}} + \underbrace{\sum_{K=1}^n N_K(\mathbf{x}) \sum_{L=1}^4 F_L(\mathbf{x}) \mathbf{c}_K^L(t)}_{\text{Near-tip Enriched}} \quad (8)$$

where n is the number of nodes per finite element, N_I represents the standard finite element interpolation functions, \mathbf{u}_I represents the nodal displacements, H is the Heaviside function, \mathbf{b}_J represents additional nodal degrees of freedom corresponding to Heaviside enrichment, F_L represents a set of enrichment functions that capture asymptotic near-tip fields, and \mathbf{c}_K represents additional nodal degrees of freedom corresponding to the near-tip enrichment. Implementation of the XFEM in Grizzly is provided by the MOOSE framework upon which Grizzly is based [32], and uses the phantom node method [33], which was shown in [34, 35] to be equivalent to the original XFEM formulation with Heaviside enrichment. Including near-tip enrichment improves the accuracy of the singular stress field and the crack front geometry representation, but reasonably accurate SIFs are still attainable when using only Heaviside enrichment with adequate mesh refinement.

An accurate way to calculate SIFs is to use domain forms of the interaction integrals. With FEM, these integrals are normally calculated in a post-processing step as a domain integral

over a finite-sized volume in the vicinity of a point on the crack front. The integrand involves combining fields from the finite element approximation with auxiliary fields from asymptotic solutions for fracture problems. The interaction integral at location s along a 3D crack front can be written as follows:

$$\begin{aligned} \bar{I}(s) = & \int_V \left[\sigma_{ij} u_{j,1}^{(aux)} + \sigma_{ij}^{(aux)} u_{j,1} - \sigma_{jk} \epsilon_{jk}^{(aux)} \delta_{1i} \right] q_{,i} dV \\ & + \int_V \left[\epsilon_{ij,1}^* \sigma_{ij}^{(aux)} - b_i u_{i,1}^{(aux)} \right] q dV \quad (9) \end{aligned}$$

where σ is the stress, u is the displacement, ϵ^* is the eigenstrain tensor, b is the vector of body forces, and q is a weight function that represents the field of virtual displacements due to the virtual crack extension. The q function is set to be 0 for the nodes inside an inner ring, and 1 for those outside an outer ring. If the selected ring radii are large enough to be outside the region of strong singularity near the crack tip, and if the mesh is sufficiently refined, the computed integrals will be independent of the ring radii. The interaction integral in Equation 9 is commonly expressed in a form that only includes the first integral and neglects body forces and thermal gradients (e.g., [2])—a form that is sufficient for many applications. The form of this integral shown here, based on [36], includes additional terms for those contributions, which are needed here to account for gradients in the imposed eigenstrains and body forces. By expressing the energy release rate in terms of the mixed-mode SIFs, the interaction integral evaluates to:

$$\begin{aligned} I(s) = & \frac{1 - \nu^2}{E} (2K_I K_I^{aux} + 2K_{II} K_{II}^{aux}) \\ & + \frac{1 + \nu}{E} (K_{III} K_{III}^{aux}) \quad (10) \end{aligned}$$

To obtain individual SIFs, the interaction integral is evaluated with different auxiliary fields. For example, by choosing $K_I^{aux} = 1.0$ and $K_{II}^{aux} = K_{III}^{aux} = 0$ and then computing $I(s)$ in Equation 9, K_I can be solved for in Equation 10.

5. Demonstration

To demonstrate the accuracy of the generalized WF approach described in Section 3, a series of simulations of various flow geometries was performed. All these simulations considered flaws in a prototypical RPV subjected to an idealized transient loading scenario. The RPV properties and loading conditions were the same in every case. For each scenario, two numerical simulations were performed: a direct simulation in which a detailed 3D model of the RPV with the flaw was run through the full transient loading history, and a WF simulation in which SIFs were generated using the methods described in this paper and then used in conjunction with stress coefficients obtained from a 1D model of the uncracked RPV. In every case, the same 3D model was used for both SIF generation and direct simulation, so the WF approach should produce results that are very close to those of the direct simulation.

5.1. Global RPV Model and BCs

The RPV geometry in all of these cases has an inner radius of 2.1971 m and a wall thickness, t , of 219.71 mm, as is prototypical of the dimensions of a pressurized-water reactor RPV. Although these RPVs have stainless steel liners on their inner surfaces, for the sake of simplicity, those liners were omitted from the model used here. The material properties of the RPV steel are in general temperature dependent; however, again for the sake of simplicity in defining the problem, they were assumed constant in this demonstration. The elastic modulus used here was 190 GPa, the Poisson's ratio was 0.3, and the thermal expansion coefficient was $13.73 \times 10^{-6} \text{ K}^{-1}$. A thermal conductivity of 41.5 W/(m K), a specific heat of 530 J/(kg K), and a density of 7833 kg/m³ were also assumed.

The stress coefficients defining the global RPV response for use with the WF approach could be computed using either a 1D, 2D, or 3D model of the RPV. With the appropriate BCs, these models have all been shown to give equivalent results when loading conditions are spatially uniform, as is the case here [26]. Because the 1D model has a significantly lower computational cost than the higher dimensional models, it was used here. The 1D model, shown in Figure 3, consisted of a row of 20 second-order line elements through the wall thickness, with 41 nodes. Biasing was used to increase the mesh density near the inner surface, where the thermal gradients are higher, so that the element size at the inner surface was 3.8 mm, and the largest element size was 23.5 mm at the outer surface.



Figure 3: 1d mesh used to compute global thermo-mechanical RPV response. Second-order elements were used, and all nodes, including mid-edge nodes are shown.

Figure 4 shows the temperature and pressure histories defining the transient used for all of these demonstration cases. At the beginning of this transient, the RPV was assumed to be under an operating temperature of 286.85°C and a pressure of 15 MPa. The transient consisted of a rapid decrease in both coolant temperature and pressure, followed by a steady increase in temperature and a spike in pressure late in the event. These are idealized transient conditions designed to subject the RPV model to both high thermal gradients and high pressures at various times throughout the transient.

Axisymmetric conditions are assumed in the thermal and mechanical models, and constraints are imposed to enforce uniform strain in the axial direction consistent with an idealization of the response as that of an infinite cylinder. The pressure history shown in Figure 4 is prescribed on the inner surface of the RPV (the left side of the 1D model), and a convective flux boundary condition was imposed on that same surface, with a constant convective heat transfer coefficient of 946.4 W/(m²K) and the coolant temperature history in Figure 4 applied as the far-field temperature.

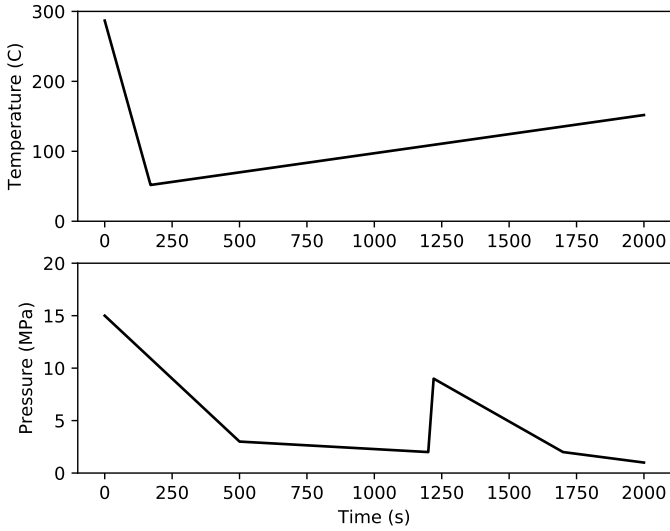


Figure 4: Coolant temperature and pressure histories that define the idealized transient conditions applied to the RPV in the demonstration cases.

5.2. Flaw Geometries and Models

A total of six scenarios with various flaw geometries are considered, with the first four of these being axis-aligned flaws. The axis-aligned flaw cases consider a circumferential surface-breaking flaw (Section 5.4), an axial surface-breaking flaw (Section 5.4), a circumferential subsurface flaw (Section 5.6), and an axial subsurface flaw (Section 5.7). The computed K_I histories for these axis-aligned scenarios were benchmarked against solutions obtained by using readily available SIFICs, as well as against solutions from another code (in Appendix B). Finally, two additional scenarios with tilted flaw geometries were considered, the first with a single off-axis flaw (Section 5.8), and the second with two interacting flaws (Section 5.9). Because in these cases the flaws were subjected to mixed-mode loading, they have nonzero values for K_I , K_{II} , and K_{III} , which are all computed with both the WF and direct solution approaches.

Figure 5 shows the flaw geometries considered here. In all cases, the flaw is a circular or semicircular flaw with a radius, a , of 17.58 mm. For the subsurface cases, the depth to the center of the flaw, d , is 43.94 mm. A flaw with these dimensions and position has the ratios $a/d = 0.4$, $d/t = 0.2$, and $a/l = 0.5$, where l is the total width of the flaw. The circumferential flaws (Figures 5a and 5c) lie in the plane containing the azimuthal and radial directions (i.e., y and x , respectively). The axial flaws (Figure 5b and 5d) lie in the plane containing the axial and radial directions of the vessel (i.e., z and x , respectively). In both the circumferential and axial cases, K_I is evaluated at the point on the flaw nearest to the inner surface of the RPV, as indicated in Figure 5. The single off-axis flaw (Figure 5e) was positioned by starting with a flaw that initially lied in the x,y plane, and was then rotated 15° about y , followed by a 15° rotation about x . The fracture integrals were evaluated at the position on the flaw with the highest axial (z) coordinate, as shown. Finally, for the case featuring two interacting off-axis flaws, fracture integrals were evaluated at the same flaw and location as was considered

in regard to the single off-axis flaw case, but a second flaw was introduced adjacent to the first flaw. The second flaw had the same size and orientation as the first, but was translated 25.0 mm in the z direction and 17.68 mm in the x direction from the location of the first flaw.

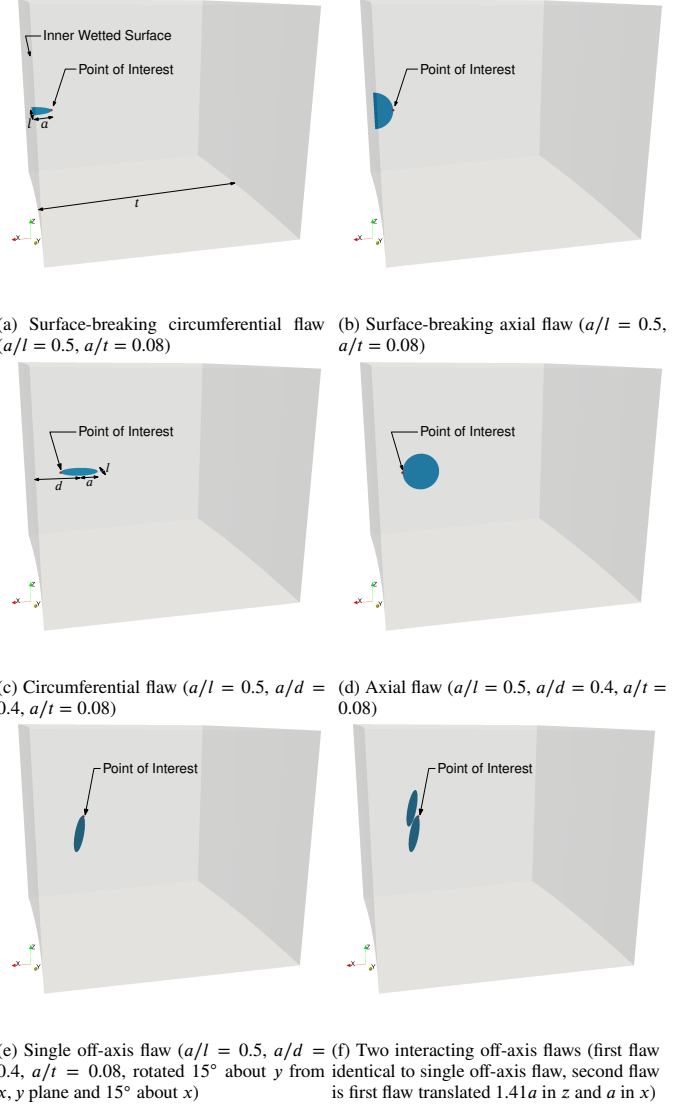


Figure 5: Flaw geometries considered in the demonstration cases. The flaws are shown in a section of the cylindrical vessel wall, and the surface shown on the left side of these sections is the inner surface, as noted. The location where fracture parameters were evaluated is indicated in each case.

In each demonstration case, the same finite element mesh was used for both SIFIC generation and the direct calculation of SIFs for a given flaw geometry. Figure 6 shows the mesh used for the subsurface circumferential flaw, and is representative of the meshes used for the other cases. A section of the RPV that is 15° azimuthally and 0.5 m in the axial direction is represented in the model, with the flaw located at the mid-plane of that section. Because the flaw is represented using XFEM, it is not explicitly included in the mesh, though the region around the flaw is significantly refined to give sufficient solution accuracy. The conformal refinement algorithm in the CUBITTM meshing

software [37] was used to locally refine the base mesh multiple times to focus the mesh refinement around the flaw. A unique mesh with refinement around the flaw was used for each case in this study.

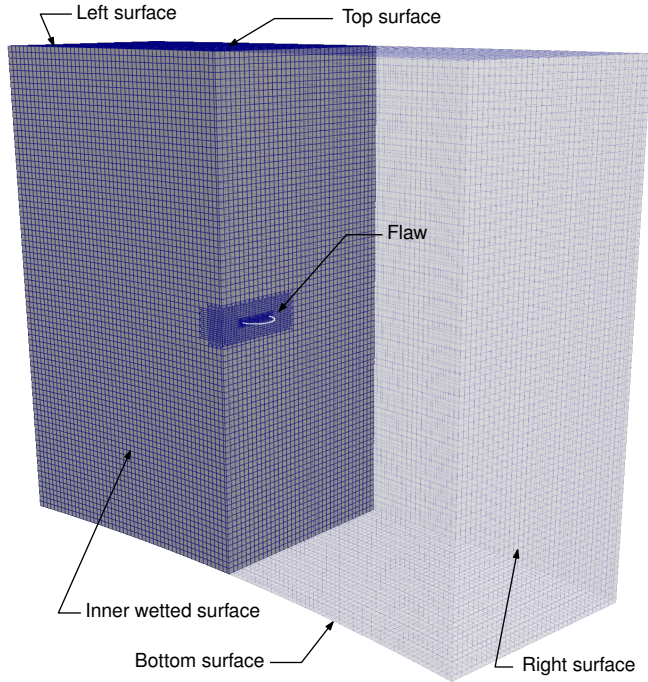


Figure 6: Cutaway view of the finite element model of a segment of the RPV wall, including a circumferential subsurface flaw. The right side of the model is translucent, allowing for visualization of the mesh refinement in the vicinity of the flaw, the face of which is superimposed on the finite element mesh here.

If the mesh is insufficiently refined in the vicinity of the flaw, the SIF variation along the flaw front can be noisy due to irregularities in the intersections between the XFEM cutting plane and the finite element mesh. This noise decreases with mesh refinement, and is also decreased significantly with near-tip enrichment. While Grizzly offers the capability to use near-tip enrichment, it was found that using increased mesh refinement with only Heaviside enrichment yielded similar accuracy for a given computational cost; thus, only Heaviside enrichment was used. This was due to the specifics of how the near-tip enrichment was implemented in the current version of this code, and may not be the case for other codes. To determine the level of mesh refinement required to obtain solutions for K_I that are sufficiently smooth and accurate, a convergence study was performed on the circumferential subsurface flaw. Figure 7 plots K_0 , the 0th order (constant) SIFIC for K_I , under spatially uniform axial stresses as a function of position on the flaw front, and compares this with the SIFIC obtained from ASME Section XI for that same flaw geometry. The ASME SIFICs are provided at three points on the flaw where these are defined. The “Level 3” refinement gives an error of less than about 1%. Similar plots for the higher-order SIFICs are provided in Appendix A, and show behavior similar to that of the constant SIFIC. Smoothing of the computed SIF as it varies along the flaw front can further improve the solutions [38], though such smoothing was not

applied here, since the accuracy of the solutions even without smoothing is sufficient for demonstrating the generalized WF approach.

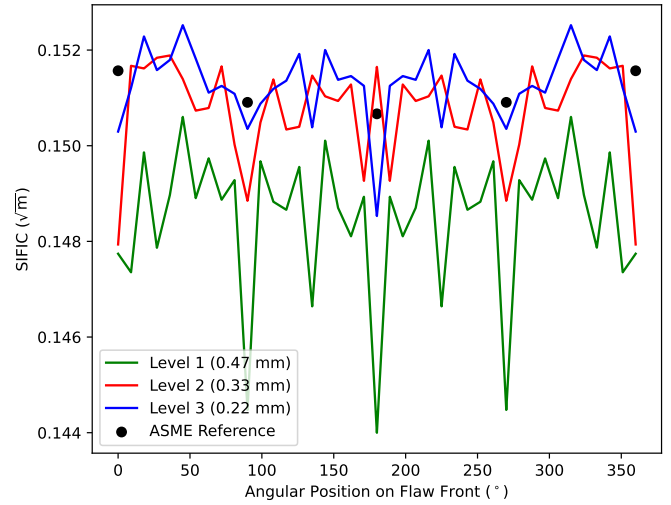


Figure 7: Convergence study on a circumferential subsurface flaw to determine the required level of mesh refinement. Variation of K_0 , the constant SIFIC, as a function of position on the crack front is shown for several mesh refinement levels, and is compared with interpolated solutions from ASME Section XI for reference. The point at an angular position of 0° is at the location nearest to the inner surface of the vessel.

Based on the findings of the above convergence study, first-order, 8-noded hexahedral meshes with refinement corresponding to “Level 3” were used for all cases. The base meshes have a nominal element size of about 6 mm, and the mesh is refined in local regions surrounding the flaw three times, each of which decreases the element size in that region by a factor of 3. With this refinement applied, the element size in the highly refined region surrounding the flaw is approximately 0.22 mm, which is approximately 1.3% of the flaw radius. The meshes for each case are unique because of the differing locations of the refinement zone, and range in size between about 600,000 and 850,000 elements.

5.3. Solution Procedures

The time histories of the fracture integrals of interest (e.g., K_I for axis-aligned flaws) over the course of the transient were computed using both the generalized WF approach and a direct calculation. In addition, for the axis-aligned flaws, histories of K_I were computed using the SIFICs from ASME Section XI as a reference solution. For both the generalized WF approach (in which SIFICs are computed using FEM) and the SIFICs from ASME Section XI, fourth-order polynomials were used, resulting in five SIFICs for each direction. A total of 200 time steps was used in the transient simulation for each model.

The solution procedure for the generalized WF approach is summarized as:

1. Using the 3D flaw model, evaluate SIFs under three orthogonal load states for each polynomial term, with ap-

appropriate BCs, as described in Section 3, to obtain the SIFs (15 in these examples).

2. Simulate the global thermo-mechanical RPV response using the 1D model and obtain polynomial coefficients for through-wall variation of axial, hoop, and radial stress for each time step in the transient (200 in these examples).
3. For each time step in the transient, use Equation 1 to compute the SIFs from the SIFs and stress coefficients.

Nearly the same procedure is taken when the ASME Section XI SIFs are used, except that instead of computing the SIFs from a 3D model in Step 1, they are computed using closed-form expressions and table lookups. Also, only 5 SIFs are calculated, and they are used together with the coefficients for the stress normal to the axis-aligned flaw. It should be noted that in the generalized WF approach, the SIFs for axis-aligned flaws corresponding to the load systems in the directions tangent to the flaw are very small compared to those normal to the flaw, but the full set of SIFs for all directions of loading is still used in each case.

The solution procedure for the direct solution is summarized as:

1. Simulate the global thermo-mechanical RPV response using the 1D model and obtain spatially varying displacement and temperature fields for each time step in the transient (200 in these examples).
2. Using the 3D flaw model, evaluate SIFs for each step in the transient, with displacements from 1D model prescribed at boundaries and temperatures from 1D model prescribed over full domain.

It would be possible to skip the first step in the above procedure, and simply use the 3D flaw model by itself to compute the response. However, applying displacements from the 1D global model to the boundaries of the 3D model simplifies the modeling approach because it eliminates the need for special constraints to keep the top surface planar while allowing free vertical movement of that surface. Displacements from the 1D model are prescribed on the left, right, top, and bottom surfaces of the 3D flaw model, as annotated on Figure 6, and the pressure load is applied to the inner wetted surface. In addition, temperatures from the 1D model are prescribed throughout the 3D flaw model, which ensures continuity of the temperature across the flaw, which is consistent with the assumptions made in the WF methods.

5.4. Circumferential Surface-Breaking Flaw

The first flaw geometry considered here is the surface-breaking circumferential flaw shown in Figure 5a. This configuration tests the SIFs generated for the loading system that involves the axial stresses, and the solutions for this flaw can be readily compared with solutions obtained using the ASME Section XI SIFs.

A comparison of the time histories of K_I from these modeling approaches is shown in Figure 8. The generalized WF approach and the direct simulation produce very similar results, indicating that this reduced order modeling procedure works correctly for surface-breaking circumferential flaws, and that these

solutions are in good agreement with the solutions using the ASME SIFs.

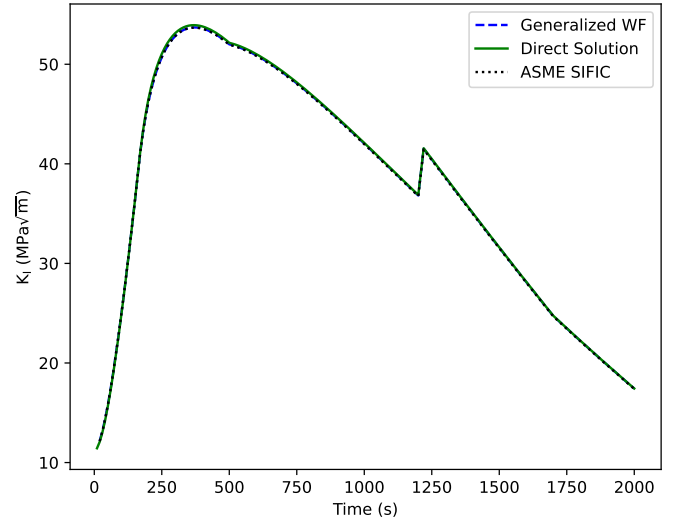


Figure 8: Time history of K_I for a circumferential surface-breaking flaw ($a/l = 0.5$, $a/t = 0.08$) under representative RPV transient loading conditions, as computed using the proposed generalized WF method, direct simulation, and SIFs from ASME Section XI.

5.5. Axial Surface-Breaking Flaw

The next case considered is the surface-breaking axial flaw shown in Figure 5b. Axial flaws test the SIFs generated for the loading system that involves the hoop stresses. In addition to the other model features tested in the circumferential surface-breaking flaw case, this case also exercises the radial body forces that are applied to enforce local equilibrium when hoop stresses are applied. The solutions for this case can also be readily compared with solutions using the ASME Section XI SIFs.

Figure 9 shows the time histories of K_I for this case, with solutions from the generalized WF approach and direct solution procedure shown together with solutions using the ASME Section XI SIFs. Similar to the first case, there is good agreement between the generalized WF and direct solutions, and these both agree well with the solution using the ASME SIFs.

5.6. Circumferential Subsurface Flaw

The next case considered is the circumferential subsurface flaw shown in Figure 5c. The time history of K_I computed for this case is shown in Figure 10. Similar to the surface-breaking cases, solutions for this flaw geometry can be readily compared with those obtained using the ASME Section XI SIFs. Throughout the transient, there is good agreement between the generalized WF and direct solution results. These solutions are both close to, but slightly lower than those obtained using the ASME SIFs. This discrepancy can be attributed to the fact that because of the alignment of the finite element mesh relative to the flaw geometry, the SIFs for the point of interest on this flaw are slightly lower than the ASME solutions

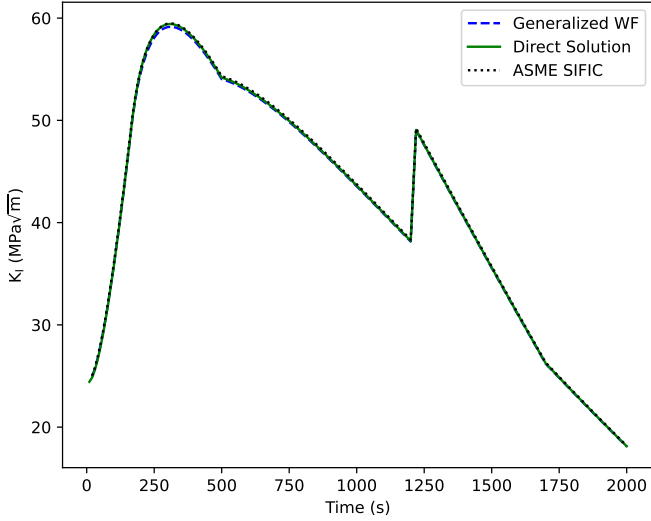


Figure 9: Time history of K_I for an axial surface-breaking flaw ($a/l = 0.5$, $a/t = 0.08$) under representative RPV transient loading conditions, as computed using the proposed generalized WF method, direct simulation, and SIFCs from ASME Section XI.

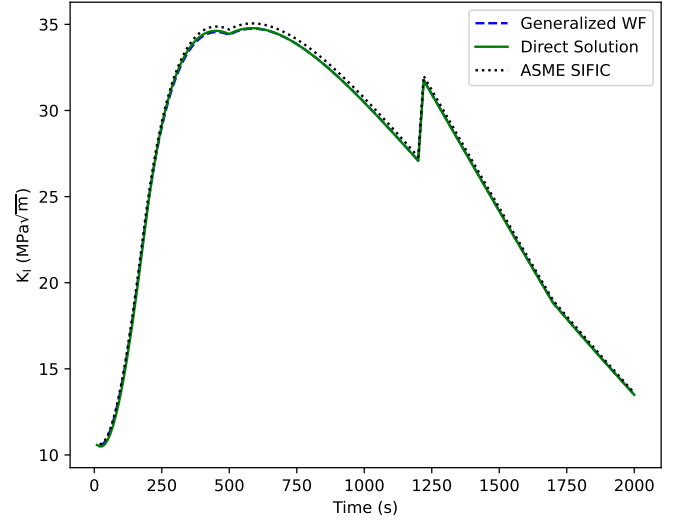


Figure 10: Time history of K_I for a circumferential subsurface flaw ($a/l = 0.5$, $a/d = 0.4$, $a/t = 0.08$) under representative RPV transient loading conditions, as computed using the proposed generalized WF method, direct simulation, and SIFCs from ASME Section XI.

(see Figures 7 and A.15 through A.18). The fact that the generalized WF and direct solutions are in good agreement indicates that the generalized WF procedure faithfully represents the solutions obtained with a given finite element mesh. The minor discrepancy between these solutions and the ASME Section XI SIFIC solution could be reduced with further mesh refinement.

It is worth noting that early in the transient, K_I is dominated by the effects of internal pressure, producing a fairly uniform stress field in the RPV. From roughly 200 to 1200 s into the transient, K_I is dominated by stresses induced by thermal gradients, but then the late pressure spike results in K_I being dominated once again by internal pressure. The difference between the solutions obtained through 3D finite element simulations in this paper and the ASME solutions is larger during times when the thermal gradient is higher, which can be attributed to slightly larger errors in the local solution for the higher-order SIFCs.

5.7. Axial Subsurface Flaw

The final axis-aligned flaw considered here is the axial subsurface flaw shown in Figure 5d. This tests the same model features as the axial surface-breaking flaw, but for a subsurface flaw geometry. The time history of K_I for this case is shown in Figure 11. This case shows behavior very similar to that for the circumferential subsurface flaw. There is good agreement between the generalized WF and direct solution results, which are both slightly lower than the solution from the ASME SIFCs, particularly at times in the transient when the thermal gradients are high. This minor discrepancy can likely be attributed to local inaccuracies in the 3D finite element model, similar to the circumferential subsurface flaw, and those errors would decrease with further mesh refinement.

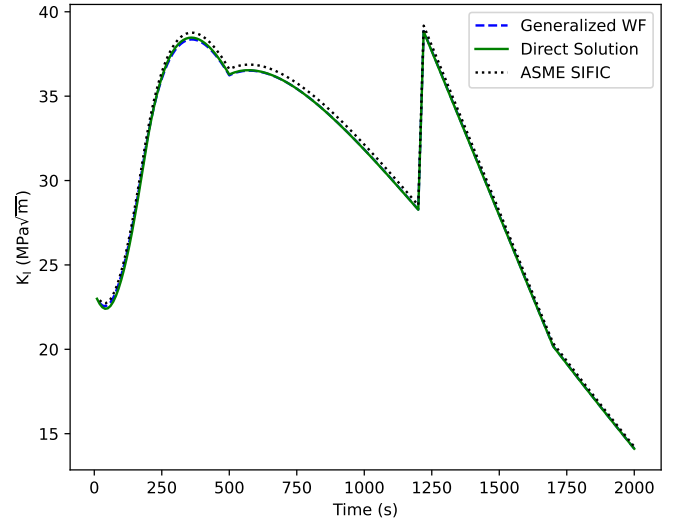


Figure 11: Time history of K_I for an axial subsurface flaw ($a/l = 0.5$, $a/d = 0.4$, $a/t = 0.08$) under representative RPV transient loading conditions, as computed using the proposed general WF method, direct simulation, and SIFCs from ASME Section XI.

5.8. Single Off-Axis Flaw

The same modeling approach used for axis-aligned flaw geometries in Sections 5.6 and 5.7 was adapted to represent the application of the generalized WF approach to a single off-axis flaw, as shown in Figure 5e. The objectives of this case were to (1) demonstrate that the generalized WF approach works on flaws for which SIFs are influenced by loading in multiple directions, and (2) to demonstrate that this approach can be used to compute other linear fracture parameters besides K_I . The flaw was intentionally rotated off the axis in two directions to induce

nonzero K_{II} and K_{III} . SIFICs were generated for K_I , K_{II} , and K_{III} by evaluating those respective quantities under the 15 loading systems required to represent fourth-order through-wall variation of the axial, hoop, and radial components of stress. Because of the lack of available benchmark solutions, only the generalized WF and direct solution approaches were compared for this flaw configuration. Figure 12 compares the time histories of K_I , K_{II} , and K_{III} for the two approaches, as evaluated at the point in the flaw nearest to the inner surface. These results show good agreement between the WF and direct solution approaches for all three of these SIFs.

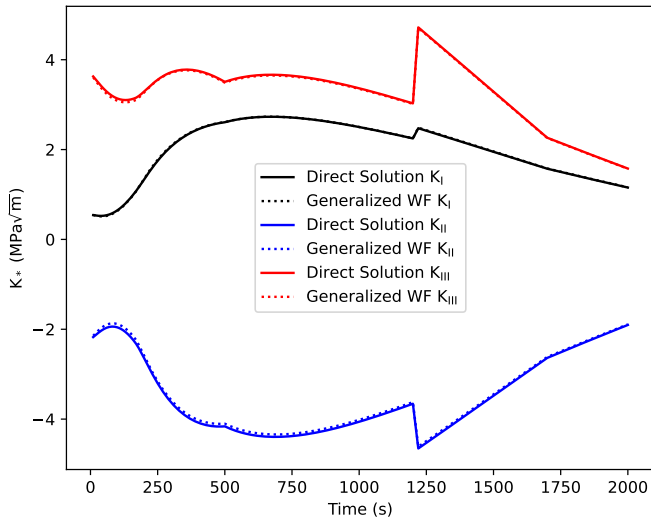


Figure 12: Time history of K_I , K_{II} , and K_{III} for a single off-axis subsurface flaw (with geometry shown in Figure 5e), as computed using the generalized WF approach and a direct solution.

5.9. Interacting Off-Axis Flaws

Finally, the generalized WF approach was applied to the problem featuring two interacting off-axis flaws, as shown in Figure 5e. If two flaws are located in close proximity in this configuration, the SIFs in one flaw under a given far-field stress state can be affected by the other flaw because it adds compliance to the system. The WF procedure for an interacting flaw scenario is essentially the same as that used for a single flaw. A FEM model that includes both flaws is subjected to the same load states, and SIFs can be evaluated at points of interest on either flaw. This approach is applied to the single off-axis flaw geometry discussed in Section 5.8, but a second flaw is added adjacent to that flaw. Both the flaws are represented using XFEM, but SIFs are only computed for one flaw.

As with the single off-axis flaw, SIFICs were generated for K_I , K_{II} , and K_{III} . Time histories of these three SIFs are shown in Figure 13 for the two approaches. For reference, this plot also shows the solutions for those same quantities for the single-flaw case are shown in this plot to highlight the significant effect that the additional compliance introduced by the second flaw has on the solution. As was the case for the single off-axis

flaw, the generalized WF and direct solution results are in good agreement for all three of these SIFs.

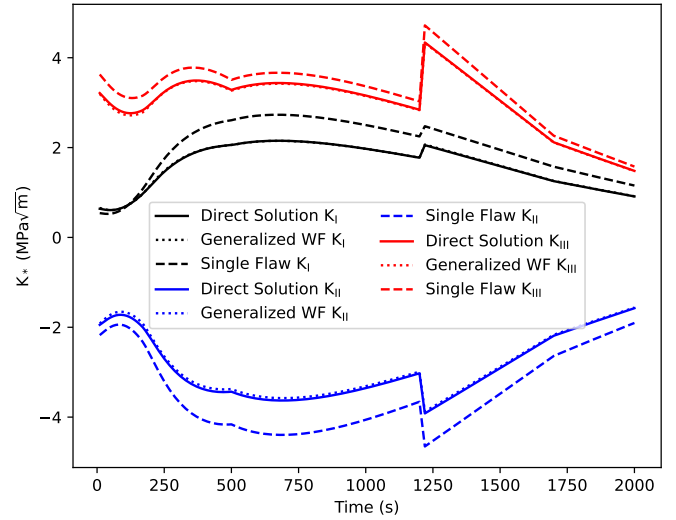


Figure 13: Time history of K_I , K_{II} , and K_{III} for an off-axis subsurface flaw in close proximity to another subsurface flaw (with geometry shown in Figure 5f), as computed using the direct solution. These are compared with the solutions for those quantities shown in Figure 12 to highlight the effect of the second flaw.

5.10. Considerations for Solution Accuracy

The results for axis-aligned and off-axis flaws presented here generally show very good agreement between directly-computed solutions and equivalent solutions computed using the generalized WF method, as well as with solutions using the ASME Section XI SIFICs where applicable. In addition, axis-aligned flaw solutions are benchmarked against solutions obtained from a separate code in Appendix B. For off-axis flaws, the XFEM-based capability to compute mixed-mode SIFs was verified against the analytical solutions of [39] in [40]. This good agreement between the generalized WF, direct, and reference solutions depends on the use of sufficiently high polynomial order in the WF solution and on the use of sufficiently refined finite element meshes, as discussed below.

The accuracy of the generalized WF solutions depends on using a polynomial of sufficiently high order to represent through-wall stress variations. All of the cases studied here used 4th order polynomials to represent the through-wall stress distribution. This was influenced by the fact that SIFICs for 4th order polynomials are provided in ASME Section XI. To explore the effects of the polynomial order on the solution accuracy, the subsurface and surface-breaking axis-aligned flaw cases were run using both 3rd and 4th order polynomials with the WF method. Figure 14 shows a comparison of the K_I histories for the surface-breaking and subsurface circumferential flaws using ASME Section XI SIFICs with these two different polynomial orders. For the surface-breaking flaw, the 3rd and 4th order solutions are nearly identical, while there is a minor but noticeable difference between the 3rd and 4th order solutions for the subsurface flaw. The same study was also performed on the axial flaws, as

well as using the generalized WF SIFICs. These results are not shown here for the sake of brevity, but similar trends were observed. These results indicate that, for the conditions explored here, a 3rd order polynomial would be sufficient for the surface-breaking flaws, while a 4th order polynomial would be recommended for subsurface flaws. The high-order polynomial terms tend to be more important for capturing the stress distribution in regions deeper in the vessel wall. The decision on the needed polynomial order for the WF method is case-specific and depends on the nature of the through-wall stress distribution.

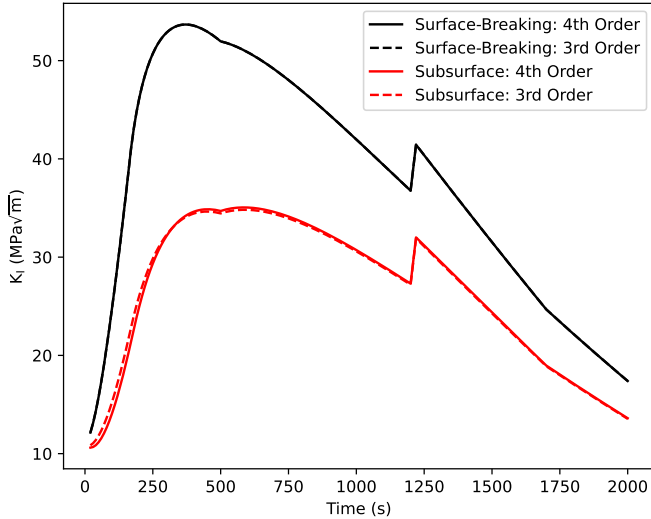


Figure 14: Time histories of K_I for the surface-breaking and subsurface circumferential flaws using the 3rd and 4th order ASME Section XI SIFICs.

The refinement of the 3D finite element mesh used for fracture mechanics calculation also significantly affects solution accuracy. If the same mesh is used for both the direct and generalized WF solutions (as was the case in this study), any errors due to insufficient mesh refinement in the flaw region would be reflected in a similar way in both of these solutions. In addition to being sufficiently refined in the flaw region (to capture near-tip stress concentrations), the mesh must also be sufficiently refined in regions away from the flaw to capture the sharp through-wall stress gradients that can occur in transient loading scenarios.

5.11. Efficiency of Generalized WF Method

Improved solution efficiency is one of the main motivations for using WF methods. The primary source of computational expense with the generalized WF method is generating the SIFICs. As previously noted, for general off-axis flaws, the detailed 3D fracture model must be evaluated for $3 \times n$ load steps, where n is the number of terms in the polynomial, so 15 load steps are required for a 4th order polynomial. Once the SIFICs are generated, the cost of evaluating SIFs under transients, which typically require hundreds of time steps, is minimal because a computationally efficient 1D model can be used for computing the global through-wall response and the cost of computing SIFs using the SIFICs is negligible. Thus, once the required number of load steps for a transient simulation exceeds the number of

load steps for SIFIC generation, the generalized WF approach would be more efficient than the direct simulation.

In practice, modeling details may make the computational expense of a SIFIC generation load step differ from that for a direct simulation. In the present study, a highly scalable parallel iterative solver was used for the direct simulations. However, this solver did not perform well with the penalty form of the inclined no-displacement BCs that were used in SIFIC generation. As a result, the SIFIC generation steps were significantly more computationally expensive than the direct simulation steps using the same finite element model. For example, for the circumferential subsurface flaw case, the average per-step cost in terms of central processing unit hours for SIFIC generation was $5.45 \times$ the per-step cost of the direct solution. Thus, the generalized WF approach, which required 15 SIFIC generation steps, reached parity in computational effort with the direct solution approach after about 82 time steps in the transient. Because 200 time steps were used in the transient studied here, the generalized WF approach was overall more efficient than the direct approach. With improvement to the boundary condition implementation, the efficiency of the SIFIC generation steps could be further improved, resulting in far greater efficiency of the generalized WF approach relative to direct solution. Even greater efficiency benefits of the generalized WF approach could be realized in cases where there is a need to analyze a flaw under a variety of transient scenarios, because once the SIFICs are generated, there is very little computational cost associated with re-using them for additional transients.

6. Summary

This paper describes a generalized WF procedure applicable to analysis of generalized flaw geometries in thin- or thick-walled cylinders. The WF approach is inherently very general, and can be used to represent the combined effects of any set of load systems on the calculation of a fracture parameter, as long as the system under consideration is linear and the principle of superposition applies. Although the WF approach is typically applied to uniaxial loading on cracks, it can be generalized to multi-axial loading scenarios, which is necessary to compute SIFs for off-axis flaws. This approach has also proven applicable to more complex geometries, such as those that arise from multiple interacting flaws.

A procedure to apply the BCs to compute SIFICs for axial, radial, and hoop components of stress in a thick-walled cylinder has been outlined here. If these three stress components are assumed to vary according to a fourth-order polynomial through the wall, SIFICs corresponding to 15 loading systems must be developed. A numerical solution approach using XFEM and interaction integrals was employed here to compute these SIFICs.

This procedure has been demonstrated and compared against direct SIF solutions for several flaw geometries, with very good agreement between the models. These SIF solutions have also been benchmarked against reference solutions by using SIFICs from ASME Section XI for the two axis-aligned flaw geometries considered.

This generalized WF approach can provide a significant benefit in terms of computational efficiency, even if it is used only to evaluate the transient response of a single flaw. To generate the SIFs requires running this model through 15 loading configurations (for the five terms of the polynomial and for the three stress directions). A typical transient simulation may require running a model through hundreds of time steps, as was the case for the examples shown herein. Once the SIFs are generated, the computational cost of evaluating K_I for a transient event, given the polynomial coefficients from a global analysis, is near zero. Thus, there can be a significant benefit in computational cost from using this procedure, even for a single transient. This makes it feasible to perform probabilistic analysis of RPVs containing multiple off-axis flaws, which would be very computationally expensive via direct simulation.

This paper only presents a methodology for computing SIFs for a specific flaw geometry. The logical next step to facilitate consideration of a wide variety of off-axis flaw geometries would be to generate a set of SIFs for a range of flaw geometries, then use methods such as multidimensional interpolation or response surface fitting to enable rapid evaluation of SIFs for other similar flaw geometries, as is done in practice for axis-aligned flaws. The parameter space is larger for off-axis flaws, but the same principles used for axis-aligned flaws are expected to apply.

Acknowledgments

This work was funded by the U.S. Department of Energy under the Light Water Reactor Sustainability (LWRS) program. This research made use of the resources of the High Performance Computing Center at Idaho National Laboratory, which is supported by the Office of Nuclear Energy of the U.S. Department of Energy and the Nuclear Science User Facilities under contract no. DE-AC07-05ID14517. The submitted manuscript has been authored by a contractor of the U.S. Government under contract no. DE-AC07-05ID14517. Accordingly, the U.S. Government retains a non-exclusive, royalty-free license to publish or reproduce the published form of this contribution, or allow others to do so, for U.S. Government purposes.

References

- [1] N. Moës, J. Dolbow, and T. Belytschko. A finite element method for crack growth without remeshing. *International Journal for Numerical Methods in Engineering*, 46(1):131–150, September 1999.
- [2] M. C. Walters, G. H. Paulino, and R. H. Dodds. Interaction integral procedures for 3-D curved cracks including surface tractions. *Engineering Fracture Mechanics*, 72(11):1635–1663, July 2005.
- [3] H. F. Bückner. A novel principle for the computation of stress intensity factors. *Z. angew. Math. Mech.*, 50:529–546, 1970.
- [4] J. R. Rice. Some remarks on elastic crack-tip stress fields. *International Journal of Solids and Structures*, 8(6):751–758, June 1972.
- [5] X.R. Wu and J. Carlsson. The generalised weight function method for crack problems with mixed boundary conditions. *Journal of the Mechanics and Physics of Solids*, 31(6):485–497, January 1983.
- [6] G.S. Wang and A.F. Blom. Weight functions and stress intensity factors for mode I cracks in arbitrary 2D geometries under general crack surface loading. *Engineering Fracture Mechanics*, 44(2):307–326, January 1993.
- [7] S.T. Yang, Y.L. Ni, and C.Q. Li. Weight function method to determine stress intensity factor for semi-elliptical crack with high aspect ratio in cylindrical vessels. *Engineering Fracture Mechanics*, 109:138–149, September 2013.
- [8] M. Beghini, L. Bertini, and V. Fontanari. Weight function for an inclined edge crack in a semiplane. *International Journal of Fracture*, 99:281–292, 1999.
- [9] M. Beghini and C. Santus. An application of the weight function technique to inclined surface cracks under rolling contact fatigue, assessment and parametric analysis. *Engineering Fracture Mechanics*, 98:153–168, January 2013.
- [10] ASME boiler and pressure vessel code, Section XI, Rules for inservice inspection of nuclear power plant components, Division 1, Rules for inspection and testing of components of light-water-cooled plants. Technical Report ASME BPVC.XI.1-2021, ASME, 2021.
- [11] *Fitness-For-Service*. Number API 579-1/ASME FFS-1. American Petroleum Institute, 2021.
- [12] S. X. Xu, R. C. Cipolla, D. R. Lee, and D. A. Scarth. Improvements in Article A-3000 of Appendix A for Calculation of Stress Intensity Factor in Section XI of the 2015 Edition of ASME Boiler and Pressure Vessel Code. *Journal of Pressure Vessel Technology*, 139(1):010801, August 2016.
- [13] R. C. Cipolla. Computational method to perform the flaw evaluation procedure as specified in the ASME Code, Section XI, Appendix A. Technical Report EPRI Report NP-1181, Failure Analysis Associates, September 1979.
- [14] K. Miyazaki, F. Iwamatsu, S. Nakanishi, and M. Shiratori. Stress Intensity Factor Solution for Subsurface Flaw Estimated by Influence Function Method. In *ASME Pressure Vessels and Piping Conference*, number PVP2006-ICPVT-11-93138, Vancouver, BC, Canada, July 23–27 2006. ASME.
- [15] Kai Lu, M. Akihiro, J. Katsuyama, Y. Li, and F. Iwamatsu. Development of Stress Intensity Factors for Subsurface Flaws in Plates Subjected to Polynomial Stress Distributions. *Journal of Pressure Vessel Technology*, 140(3), June 2018.
- [16] G. R. Irwin. Crack-extension force for a part-through crack in a plate. *Journal of Applied Mechanics*, 29(4):651–654, December 1962.
- [17] J. C. Newman Jr. and I. S. Raju. Stress-intensity factor equations for cracks in three-dimensional finite bodies. Technical Report NASA Technical Memorandum 83200, National Aeronautics and Space Administration, August 1981.
- [18] M. Isida and H. Noguchi. Tension of a plate containing an embedded elliptical crack. *Engineering Fracture Mechanics*, 20(3):387–408, January 1984.
- [19] T.L. Dickson, P. T. Williams, B. R. Bass, and H. B. Klasky. Fracture Analysis of Vessels – Oak Ridge, FAVOR, v16.1, computer code: User’s guide. Technical Report ORNL/LTR-2016/310, Oak Ridge National Laboratory, Oak Ridge, TN, September 2016.
- [20] P.T. Williams, T.L. Dickson, B. R. Bass, and H. B. Klasky. Fracture Analysis of Vessels – Oak Ridge, FAVOR, v16.1, computer code: Theory and implementation of algorithms, methods, and correlations. Technical Report ORNL/LTR-2016/309, Oak Ridge National Laboratory, Oak Ridge, TN, September 2016.
- [21] Electrabel. Safety case report: Doel 3 - reactor pressure vessel assessment. Technical report, Electrabel, December 2012.
- [22] FANC (Federal agentschap voor nucleaire controle). Doel 3 and Tihange 2 reactor pressure vessels: Provisional evaluation report. Technical report, FANC, January 2013.
- [23] B. R. Bass, T. L. Dickson, S. B. Gorti, H. B. Klasky, R. K. Nanstad, M. A. Sokolov, and P. T. Williams. ORNL evaluation of Electrabel safety cases for Doel 3 / Tihange 2: Final report (R1). Technical Report ORNL/TM-2015/59349, Oak Ridge National Laboratory, Oak Ridge, TN, November 2015.
- [24] V.F. González-Albuixech, G. Qian, and M. Niffenegger. Integrity analysis of reactor pressure vessels subjected to pressurized thermal shocks by XFEM. *Nuclear Engineering and Design*, 275:336–343, August 2014.
- [25] V. F. González-Albuixech, G. Qian, and M. Niffenegger. Integrity analysis of a reactor pressure vessel with quasi laminar flaws subjected to pressurized thermal shocks. *Nuclear Engineering and Design*, 280:464–472, December 2014.
- [26] B.W. Spencer, W.M. Hoffman, and M.A. Backman. Modular system for probabilistic fracture mechanics analysis of embrittled reactor pressure

- vessels in the Grizzly code. *Nuclear Engineering and Design*, 341:25–37, January 2019.
- [27] B. W. Spencer, W. M. Hoffman, S. Biswas, W. Jiang, A. Giorla, and M. A. Backman. Grizzly and BlackBear: Structural component aging simulation codes. *Nuclear Technology*, 207(7):981–1003, April 2021.
- [28] T. Mura. General theory of eigenstrains. In S. Nemat-Nasser and G. Æ. Oravas, editors, *Micromechanics of defects in solids*, volume 3, pages 1–73. Springer Netherlands, Dordrecht, 1987.
- [29] A. P. Boresi, R. J. Schmidt, and O. M. Sidebottom. *Advanced Mechanics of Materials, 5th Edition*. Wiley, 1993.
- [30] T. Belytschko and T. Black. Elastic crack growth in finite elements with minimal remeshing. *International Journal for Numerical Methods in Engineering*, 45(5):601–620, June 1999.
- [31] N. Moës, J. Dolbow, and T. Belytschko. A finite element method for crack growth without remeshing. *International Journal for Numerical Methods in Engineering*, 46(1):131–150, 1999.
- [32] W. Jiang, B. W. Spencer, and J. E. Dolbow. Ceramic nuclear fuel fracture modeling with the extended finite element method. *Engineering Fracture Mechanics*, 223:106713, January 2020.
- [33] A. Hansbo and P. Hansbo. A finite element method for the simulation of strong and weak discontinuities in solid mechanics. *Computer Methods in Applied Mechanics and Engineering*, 193(33-35):3523–3540, Aug 2004.
- [34] P.M.A. Areias and T. Belytschko. A comment on the article “A finite element method for simulation of strong and weak discontinuities in solid mechanics” by A. Hansbo and P. Hansbo *Comput. Methods Appl. Mech. Engrg.* 193 (2004) 3523-3540. *Computer Methods in Applied Mechanics and Engineering*, 195(9-12):1275–1276, 2006.
- [35] J.-H. Song, P. M. A. Areias, and T. Belytschko. A method for dynamic crack and shear band propagation with phantom nodes. *International Journal for Numerical Methods in Engineering*, 67(6):868–893, 2006.
- [36] T. Nakamura and D. M. Parks. Determination of elastic T-stress along three-dimensional crack fronts using an interaction integral. *International Journal of Solids and Structures*, 29(13):1597 – 1611, 1992.
- [37] M. Parrish, M. Borden, M. Staten, and S. Benzley. A selective approach to conformal refinement of unstructured hexahedral finite element meshes. In *Proceedings of the 16th International Meshing Roundtable*, pages 251–268. Springer Berlin Heidelberg, 2006.
- [38] B. W. Spencer, W. M. Hoffman, A. Jain, S. Biswas, and S. L. N. Dhulipala. Reactor pressure vessel fracture mechanics development and concrete application testing for Grizzly. Technical Report INL/EXT-21-64522, Idaho National Laboratory, September 2021.
- [39] H. Tada, P. C. Paris, and G. R. Irwin. *The Stress Analysis of Cracks Handbook, Third Edition*. ASME Press, 2000.
- [40] J. Dolbow, Z. Zhang, B. Spencer, and W. Jiang. Fracture capabilities in Grizzly with the eXtended Finite Element Method (X-FEM). Technical Report INL/EXT-15-36752, Idaho National Laboratory, Idaho Falls, ID, September 2015.

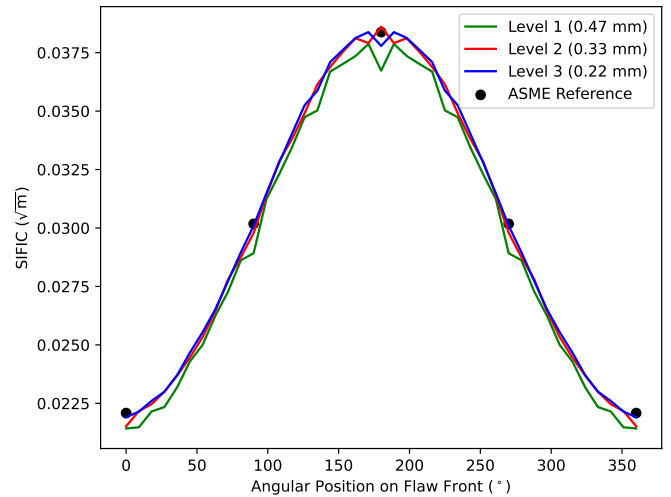


Figure A.15: Convergence study of a circumferential subsurface flaw showing variation of K_1 , the linear SIFIC, as a function of position on the crack front for several mesh refinement levels, with comparison to reference ASME Section XI solutions.

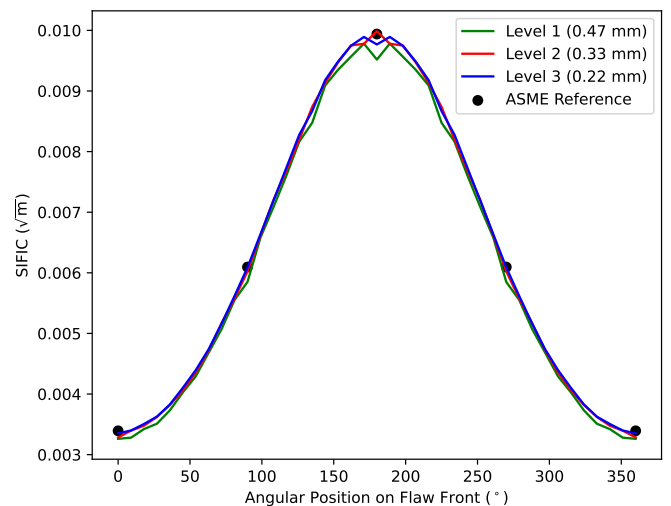


Figure A.16: Convergence study on a circumferential subsurface flaw showing variation of K_2 , the quadratic SIFIC, as a function of position on the crack front for several mesh refinement levels, with comparison to reference ASME Section XI solutions.

Appendix A. Mesh Convergence Study: Higher-Order Terms

A convergence study to assess the needed mesh refinement level in the vicinity of the circumferential subsurface flaw shown in Figure 5c was presented in the body of the paper. Plots of the constant SIFIC as a function of angular position on the flaw front were shown for various mesh refinement levels in Figure 7. For completeness, similar plots for the first- through fourth-order terms are shown in Figures A.15 through A.18. The relative errors are relatively consistent across the SIFIC orders.

Appendix B. Solution Benchmarking: Axis-Aligned Flaws

The generalized WF solutions for axis-aligned flaws in Sections 5.4 through 5.7 were compared with direct solutions as well as with solutions obtained using Grizzly with the ASME

Section XI SIFICs. In all cases, there was good agreement between these solutions. For an additional comparison of these solutions with reference solutions, these same models were run using FAVOR Version 16.1. The solution approach taken by FAVOR and Grizzly are similar in that a 1D axisymmetric model was used for the global thermo-mechanical response. For axis-aligned flaws with the dimensions studied here, FAVOR uses the ASME Section XI SIFICs, while for subsurface flaws, FAVOR uses the pre-2015 ASME Section XI approach based on membrane and bending stresses using the approach of [13] for computing correction factors.

As shown in Figure B.19, there is very good agreement be-

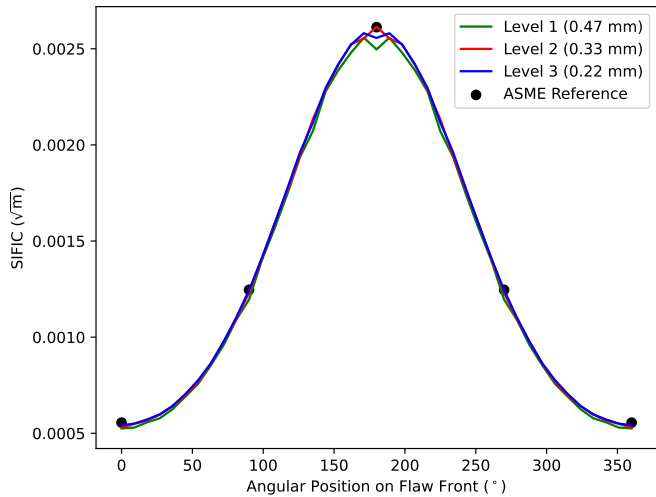


Figure A.17: Convergence study of a circumferential subsurface flaw showing variation of K_3 , the cubic SIFIC, as a function of position on the crack front for several mesh refinement levels, with comparison to reference ASME Section XI solutions.

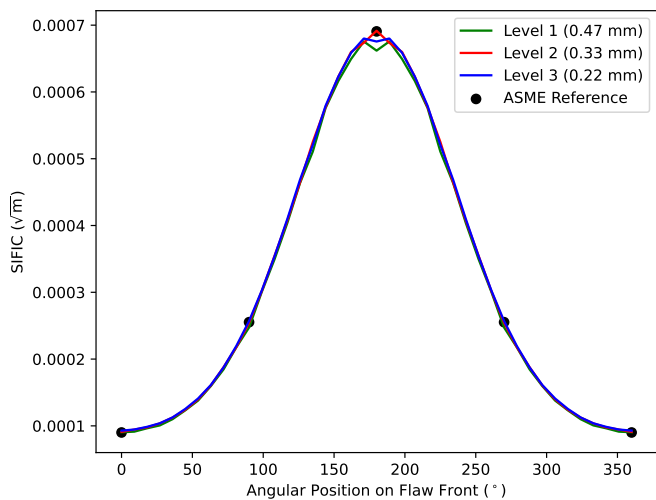


Figure A.18: Convergence study of a circumferential subsurface flaw showing variation of K_4 , the quartic SIFIC, as a function of position on the crack front for several mesh refinement levels, with comparison to reference ASME Section XI solutions.

tween the Grizzly and FAVOR solutions for the surface-breaking circumferential flaw. Figure B.20 shows a similar comparison between Grizzly and FAVOR solutions for the subsurface circumferential flaw. In this case, the Grizzly solution using the current ASME Section XI SIFCs is somewhat higher than the FAVOR solution, which is not entirely unexpected because FAVOR uses the pre-2015 ASME Section XI method. Grizzly also has an option to use that method, which is implemented by sampling the polynomial describing the through-wall stress variation at the inner and outer points on the flaw and using that to compute the membrane and bending stresses. The Grizzly solution using the pre-2015 ASME method in that way, also

shown, agrees much more closely with the FAVOR solution. Axial surface-breaking and subsurface flaws were also modeled with both codes. These results are not shown for brevity, but trends very similar to those for circumferential flaws were also observed.

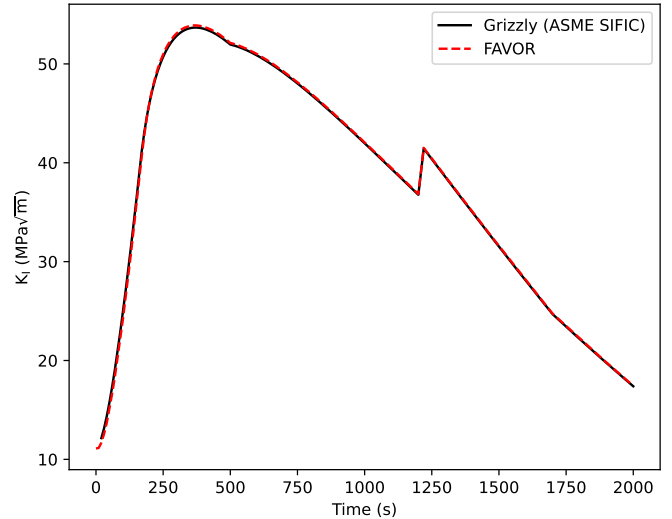


Figure B.19: Comparison of time histories of K_I for the surface-breaking circumferential flaw computed by Grizzly (using the ASME Section XI SIFCs) and FAVOR.

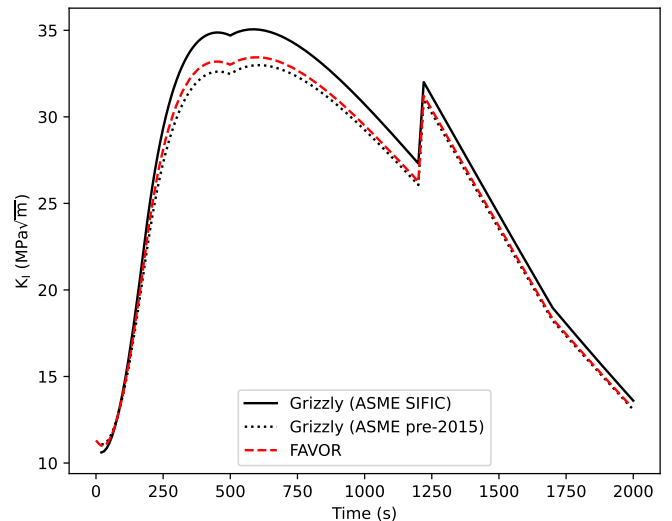


Figure B.20: Comparison of time histories of K_I for the subsurface circumferential flaw computed by Grizzly and FAVOR. Grizzly solutions are shown using both the current ASME Section XI SIFCs for subsurface flaws and the pre-2015 ASME Section XI method.

In this particular case, the pre-2015 ASME Section XI solutions are less conservative than the current ASME Section XI method, but for other cases they are overly conservative. Based on the authors' experience [38], the current ASME Section XI solutions match well with the results from detailed 3D finite element simulations similar to those presented in this paper across

a range of flaw geometries, and are preferred over the pre-2015 ASME Section XI method.

Once the differences between K_I solution methods are taken into account, this comparison between the code used in the present study and another code shows good agreement and builds confidence in the accuracy of the solutions presented here.